TISSUE ENGINEERING: Part A Volume 26, Numbers 5 and 6, 2020 © Mary Ann Liebert, Inc. DOI: 10.1089/ten.tea.2019.0237



ORIGINAL ARTICLE

Process–Structure–Quality Relationships of Three-Dimensional Printed Poly(Caprolactone)-Hydroxyapatite Scaffolds

Sam Gerdes, BSc,^{1,*} Azadeh Mostafavi, MSc,^{1,*} Srikanthan Ramesh, MSc,² Adnan Memic, PhD,^{1,3,4} Iris V. Rivero, PhD,² Prahalada Rao, PhD,¹ and Ali Tamayol, PhD^{1,3}

Bone defects are common and, in many cases, challenging to treat. Tissue engineering is an interdisciplinary approach with promising potential for treating bone defects. Within tissue engineering, three-dimensional (3D) printing strategies have emerged as potent tools for scaffold fabrication. However, reproducibility and quality control are critical aspects limiting the translation of 3D printed scaffolds to clinical use, which remain to be addressed. To elucidate the factors that yield to the generation of defects in bioprinting and to achieve reproducible biomaterial printing, the objective of this article is to frame a systematic approach for optimizing and validating 3D printing of poly(caprolactone) (PCL)-hydroxyapatite (HAp) composite scaffolds. We delineate the effect of PCL-to-HAp ratio, print velocity, print temperature, and extrusion pressure on the architectural and mechanical properties of the 3D printed scaffold. Furthermore, we present an *in situ* image-based monitoring approach to quantify key quality-related aspects of constructs, such as the ability to deposit material consistently and print elementary shapes with fewer flaws. Our results show that small defects generated during the printing process have a significant role in lowering the mechanical properties of 3D printed polymeric scaffolds. In addition, the *in vitro* osteoinductivity of the fabricated scaffolds is demonstrated.

Keywords: 3D printing, bone tissue scaffolds, poly(caprolactone) (PCL)-hydroxyapatite (HAp) composites, *in situ* imaging, osteoinductivity

Impact Statement

Identifying quality control measures is essential in the translation of three-dimensional (3D) printed scaffolds into clinical practice. In this article, we highlighted the importance of selected printing parameters on the quality of the 3D printed scaffolds. We also demonstrated that flaws, such as voids, significantly lower the mechanical properties (compressive modulus) of 3D printed polymeric scaffolds.

Introduction

B ONE DEFECTS ARE common and can be caused by trauma, tumors, and diseases. Critically sized defects overwhelm the regenerative properties of the native tissue and typically do not heal. Current treatments are primarily based on the use of autografts and allografts. However, these clinical approaches have significant limitations due to donor site morbidity and possible pathogenic immune responses in autografts and allografts, respectively. An al-

ternative approach focuses on the engineering of functional tissue constructs by combining scaffolds, cells, and signaling cues.⁴ These activities have mainly centered on the understanding and regulating of the interactions of cells, biomaterials, and biological factors.⁵

Scaffolds have become a central platform for achieving the desired interactions between various cells and substrates. ¹⁻³ As a result, various technologies such as electrospinning, micromolding, biotextiles, and three-dimensional (3D) printing (additive manufacturing) have been developed for the

¹Department of Mechanical and Materials Engineering, University of Nebraska-Lincoln, Lincoln, Nebraska.

²Department of Industrial and Systems Engineering, Rochester Institute of Technology, Rochester, New York.

³Department of Biomedical Engineering, University of Connecticut, Farmington, Connecticut.

⁴Center of Nanotechnology, King Abdulaziz University, Jeddah, Saudi Arabia.

^{*}These two authors contributed equally to this study.

fabrication of scaffolds with biomimetic physicochemical properties and architectural features. Among these techniques, 3D printing has shown to be the most versatile in engineering structures with biomimetic architectures. In the past few years, a multitude of 3D printing and bioprinting strategies have been developed and characterized for tissue engineering applications. 4,12,13

The goal of this research is to predict the architectural features of the 3D printed scaffolds of clinically relevant dimensions and minimize flaws generated during the printing process. In pursuit of this goal, we quantify the effect of process parameters on the geometry and functional quality (mechanical and biological properties) of the construct in the context of extrusion-based 3D printing of poly(caprolactone) (PCL)-hydroxyapatite (HAp) composite scaffolds. Among various 3D printing approaches, the use of extrusion-based printers has garnered predominant application for engineering scaffolds from biopolymers and osteogenic materials with physical properties comparable to bone tissue.^{4,14} The relative simplicity, low cost, and large supply of extrusion-based printers have contributed to this trend. 15 Apart from cost, extrusion-based printing accommodates a large variety of materials, ranging from hydrogels and soft polymers to thermoplastic materials.

PCL is one of the most popular biopolymers for bone tissue engineering, as this Food and Drug Administration-approved thermoplastic polymer offers a slow degradation rate (ranging from months to a few years), which is comparable to the rate of bone regeneration. While biocompatible, PCL is not osteoinductive. Furthermore, PCL does not mimic the composition of native bone extracellular matrix (ECM) and its mechanical strength and compressive modulus are inferior compared to typical bone tissue. Consequently, PCL is typically mixed with bioceramics, bioglasses, or biological factors to improve the rate of osteogenesis. ^{2,3,6}

HAp is a mineral natively produced in bone tissue, and is a large constituent of the bone matrix, with the other major constituent being collagen. While both HAp and collagen are biocompatible, they serve different functions in bone ECM, as they are responsible for the overall hardness and flexibility, respectively. 18 Furthermore, because HAp is osteoinductive, it has been widely used in the fabrication of bone scaffolds. ^{19,20} The incorporation of HAp typically improves the mechanical properties of PCL, approaching the physical properties of native bone tissue. 19 As a result, in this study, we focused on 3D printing of PCL and HAp composites; PCL/HAp composites have been previously used in bone tissue engineering. For example, PCL and HAp scaffolds have been successfully 3D printed and tested to induce osteogenesis both in vitro and in vivo.²¹ However, the present challenge is to ensure the reliability, predictability, and reproducibility of 3D printing composites through *in situ* quality monitoring and control. ^{22–24}

Researchers have optimized extrusion-based 3D printing parameters, such as composition, print speed, extrusion pressure, temperature, and outer needle diameter for printing bone scaffold material through statistical experimentation. Quality assurance of this nature can be separated into layer-level and part-level aspects, where a layer-level approach typically investigates strand characteristics—a strand is a single line or track of deposited material. At the part level, the emphasis is on quantifying layer interactions and building

geometric quality (architecture). Key literature in the area is reviewed in this study, in the context of research needs.

To evaluate the layer-level effects of printing parameters on the strand characteristics, Kang *et al.* varied needle diameter, pressure, layer height, and print speed for several hydrogel compositions, while comparing the printed pathways to their ideal width, height, and length. They report that increasing the printing pressure increased the flow rate, resulting in a larger width and height in the printed strands. However, the average strand width was determined by dividing the average construct width by the number of deposited strands, rather than through direct measurement of each strand. This procedure is the key to understanding one of Kang *et al.* 's²⁵ conclusion that linear print speed did not affect the strand width. The current lack of precise *in situ* measurement of strand quality substantiates the need for sensor-based process monitoring.

In contrast, definite trends of decreasing strand width with increasing linear print speed were shown in a few studies. ^{26–28} Notably, Webb and Doyle further quantified the layer-level printability through varying the linear print speed, pressure, and needle diameter to assess the strand width of the created paths. ²⁷ They observed that strand width was correlated with pressure, and negatively correlated with linear print speed. In addition, Webb and Doyle ²⁷ note that at high pressures, changes in linear print speed have a more dramatic effect on strand width, whereas, at lower pressures, the print speed has a largely linear and directly proportional relationship with strand width.

On the part-level scale, quantification of the intentionally printed pore shapes can be achieved through the relationship illustrated by Ouyang *et al.*²⁹ and Soltan *et al.*,³⁰ which links the area and the perimeter of a pore. Derived from circularity, a secondary dimensionless measurement presented in the works of Ouyang *et al.*²⁹ and Soltan *et al.*³⁰ allows for the quantification of the pore shape, with an ideal value of one denoting an ideal square-shaped pore.

To address the growing need for *in-situ* process monitoring and quantification of the process–structure–property relationship in the 3D printing of bone tissue scaffolds, the objectives of this work are as follows. First, an extrusion-based bioplotter is used to print PCL/HAp composites in the form of single strands, as well as scaffolds with three different geometries. Second, we quantify the effect of process variables, namely pressure, temperature, and linear print speed on the dimension and shape fidelity of the deposited strand. These assessments are made using *in situ* optical imaging and analysis. Third, we assess the physical and biological effectiveness of 3D printed bone scaffolds in bone tissue engineering through mechanical testing and *in vitro* culture of human mesenchymal stem cells (hMSCs).

Materials and Methods

Materials

Materials, including PCL (Mw=14,000 Da) and HAp (2.5 μ m powder), were purchased from Sigma-Aldrich (MO) and were used as received, unless mentioned otherwise. hMSCs and the growth culture medium were purchased from RoosterBio (MD). Cell culture reagents were purchased from Thermo-Fisher.

Preparation of materials for 3D printing

PCL/HAp composites were formed by mixing the components by weight ratio to achieve the desired material compositions of 90/10, 80/20, 70/30, and 60/40 (%PCL/%HAp w/w). The mixtures were then heated to 100°C to melt the PCL before manual stirring to homogenize the material.

Printing of composite scaffolds

Printing was conducted using an extrusion-based 3D printer, a 3D-Bioplotter (manufacturer series) from EnvisionTEC (Gladbeck, Germany), shown in Figure 1b. With this bioplotter, it is possible to customize a large number of printing variables, such as linear print speed, pressure, print head temperature, bed temperature, infill pattern and spacing, preflow, postflow, vertical needle offset, and needle size, among others.

After preparation, the material was loaded into a stainless steel syringe barrel, melted at a process condition-dependent temperature, and pneumatically extruded through a $700\,\mu m$ outer diameter stainless steel nozzle at a condition-dependent pressure. Following the cooling and solidification of the PCL/HAp composite, *in situ* imaging of the layer was conducted with an optical camera built into the machine, as shown in Figure 1c. Based on extensive screening tests, we

report the effect of linear print speed for each of the four PCL/HAp compositions (90/10, 80/20, 70/30, and 60/40) at the following four temperature and pressure combinations in uniform increments: 110°C and 1.5 bar, 120°C and 2.5 bar, 130°C and 3.5 bar, and 140°C and 4.5 bar. This results in a total of 16 possible composition-pressure-temperature combinations. However, not all of these combinations produce constructs of desirable strand and shape quality.

In-situ monitoring and quantification of print quality

To assess the geometric quality of the constructs printed at the viable process conditions, three types of shapes, namely, circle, square, and triangle, were printed without infill, and the inner and outer edges were assessed for circularity in ImageJ. Circularity was determined by using the following equation^{29,30}:

$$C = (4\pi \times A)/P^2 \tag{1}$$

where C is circularity (dimensionless), A is the area of the shape (mm²), and P is its perimeter (mm). Five replicates of each shape were printed, each with 2 circularity measurements (inner and outer edge), giving 10 circularity measurements for each shape, which were then averaged.

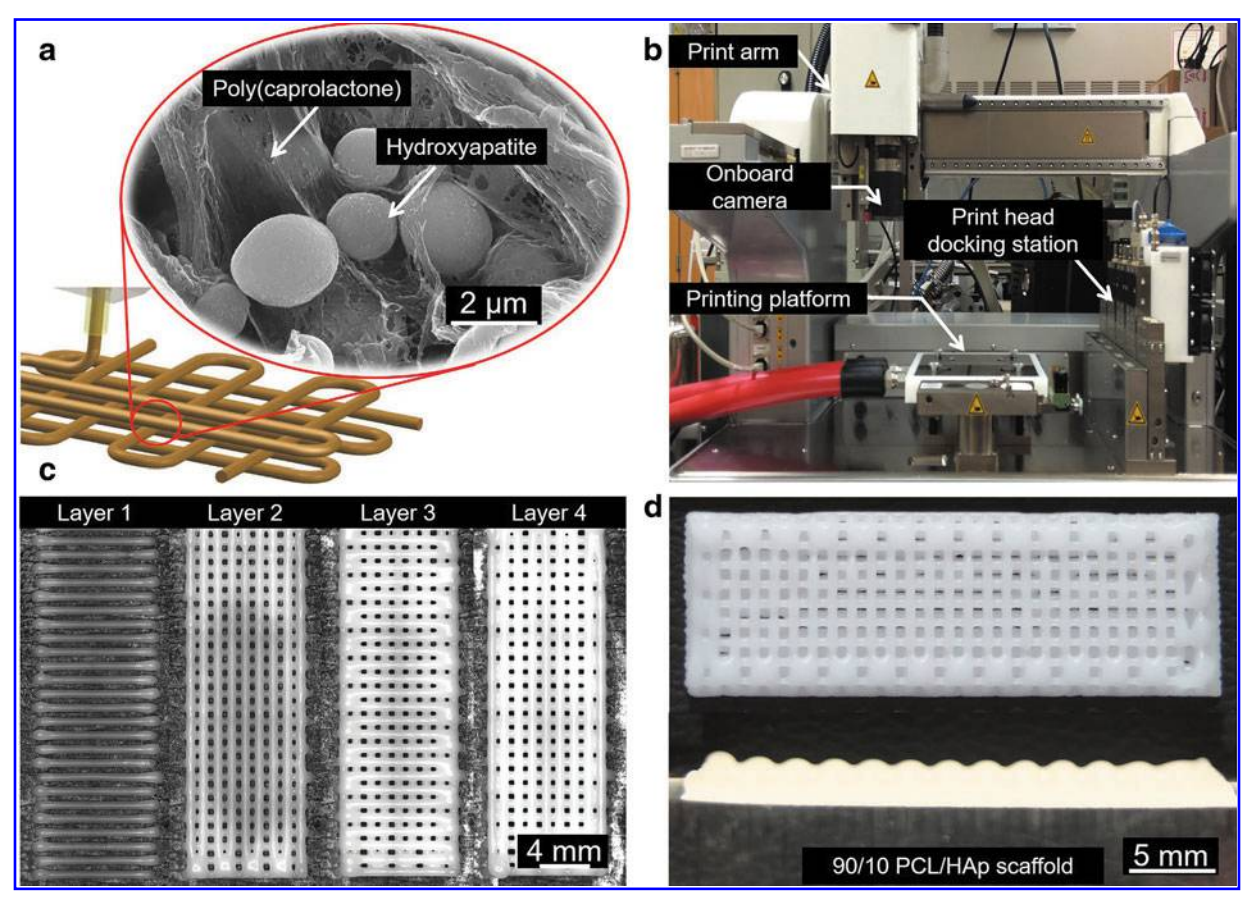


FIG. 1. 3D printing of PCL/HAp scaffolds and the *in situ* monitoring of the geometrical outcome. (a) Schematic of PCL/HAp printing and microstructure of interspersed HAp in the thermoplastic PCL. (b) Print setup of the bioplotter used in the study and the location of the camera for *in situ* monitoring of the printing process. (c) Layer by layer images generated through *in situ* monitoring. (d) A representative image of a 3D printed PCL/HAp scaffold with clinically relevant dimensions. 3D, three dimensional; PCL, poly(caprolactone); HAp, hydroxyapatite.

We have adopted a stepwise optimization approach. First, we ascertain the feasible linear print velocity setting for a particular composition, nozzle temperature, and pressure by comparing the strand width to the desired width of the outer nozzle diameter (700 mm) through in situ imaging. For this purpose, five lines (strands) were printed at different linear print speeds for a fixed composition, temperature, and pressure, and the strands were imaged immediately following deposition using the in situ optical imaging. The width of the strand was then characterized at seven approximately equidistant points along its length using the open-source software (ImageJ). The strand width measurements were averaged, and a desirable linear print speed was chosen from the plot of average strand diameter versus linear print speed. Lastly, once the feasible linear print velocity settings were determined for a particular nozzle temperature, and pressure composition, we then studied print quality from a geometric perspective.

Mechanical characterization

Rheological testing. Rheological properties of the developed composites were assessed using a rotational rheometer. An HR-3 Discovery Series Hybrid Rheometer from TA Instruments (New Castle, DE), equipped with an advanced Peltier Plate system, was used in combination with a 20 mm smart SWAP parallel plate geometry. All of the experiments were done using a measurement gap set at 500 μm . An amplitude sweep was first performed for the 70/30 PCL/HAp at 110°C to identify the linear viscoelastic region (LVR). A strain percentage within the LVR was used to perform all the subsequent oscillatory experiments.

For the frequency sweep experiments, the composites were subjected to angular frequencies ranging from 0.5 to 100 rad/s at all the extrusion temperatures (110°C, 120°C, 130°C, and 140°C). The shear-thinning behavior of the composites was quantified by applying the power law ($\eta = K\dot{\gamma}^{(n-1)}$) equation to the double log plot of complex viscosity (η) and shear rate ($\dot{\gamma}$) after transforming the data using the Cox-Merz rule for polymer melts. All the experiments were performed using three independent samples.

Compressive testing. The rigidity of the samples was assessed in terms of the compressive modulus of printed $10\,\mathrm{mm} \times 10\,\mathrm{mm} \times 2.5\,\mathrm{mm}$ samples (completely solid). The results from the 3D printed samples were compared with identical sized molded samples. Four samples were prepared with theoretically solid box architectures for both the lowest and highest temperature and pressure print conditions for each composition at its desirable linear print speeds. Compression testing was conducted using a Cellscale Univert from Cellscale (Canada) to a maximum strain of 7–8% over a minute for the molded and printed samples, respectively. The compressive modulus was determined as the slope of the linear region of the stress-strain curve.

Biological property characterization

To evaluate the bioactivity of the materials, hMSCs (RosterBio MSC-003) were cultured on the samples, and their viability, attachment, and potential for differentiation to osteoblasts were assessed. First, samples were prepared by printing the material using the bioplotter. The samples

were printed to have four layers and final dimensions of 10 mm×10 mm×2.4 mm. Printed samples were then sterilized under UV light, immersed in 70% ethanol, and washed with phosphate-buffered saline (PBS). The hMSCs were expanded in their complete growth media made of minimum essential medium α supplemented with 16% (v/v) fetal bovine serum, 2 mM L-glutamine, 100 U/mL penicillin, and 100 ng/mL streptomycin, and incubated at 5% CO₂ and 37°C. Cells were passaged every 3–4 days at ~80% confluence with trypsin-ethylenediaminetetraaceticacid (0.1%), and their media were changed every 2 days. The hMSCs were subsequently harvested at passage 5 and cultured on sterilized samples by the concentration of 300 cells/mm², and maintained in the complete growth media for further experiments.

Cell attachment and viability. The viability and proliferation rate of hMSCs were quantified by measuring their metabolic activities using PrestoBlue Cell Viability Reagent (Invitrogen) on days 1, 3, and 7 after culturing on the samples and maintaining in complete growth media. At each measurement time point, samples were incubated in a solution of 10% (v/v) PrestoBlue reagent in growth media in the incubator at 37°C for 1 h. The fluorescence intensity of the solution was measured using a Cytation 5 Cell Imaging Multi-Mode Reader (Biotek) at 540 nm (excitation)/600 nm (emission). Samples were washed with PBS and maintained in fresh growth media for measurement at the next time point.

The attachment of cells on the surface of the scaffolds and their morphology were investigated by scanning electron microscopy (SEM) imaging of cells cultured on the scaffold. Cell-cultured constructs were fixed in 2.5% (v/v) glutaral-dehyde in PBS for 2 h and washed twice with PBS. Samples were dehydrated with a graded ethanol series and then dried in a desiccator. The samples were sputtered by a thin layer of gold and then analyzed by an SEM (FEI Quanta 200 Environmental).

Assessment of cellular differentiation and mineralization. After 3 days of hMSC culture on the samples, the growth media were changed to differentiation media composed of complete growth media supplemented with $10\, nM$ dexamethasone (Sigma), $10\, mM$ β -glycerophosphate (Sigma), and $50\, \mu g/mL$ L-ascorbic acid (Sigma). The differentiation medium was changed every 3–4 days, and the cells were kept for 35 days after starting their differentiation for further investigation.

Immunostaining. Since the main goal of this study was to assess the effect of process parameters on the printing quality, we wanted to ensure the osteoconductivity of the printed scaffolds, rather than to compare different conditions. While assessment of gene expression could be used as a tool for the evaluation of osteodifferentiation, we monitored alkaline phosphatase (ALP) expression, osteogenic marker expression, and calcium deposition, which are more important indicators of cellular differentiation. For proper comparison of the role of scaffold composition on cellular differentiation, gene expression analysis should be carried out in future.

On day 28 postdifferentiation, cell-seeded constructs were fixed by 4% (w/v) paraformaldehyde for 15 min, and then permeabilized by 0.3% (v/v) triton 100×for 10 min. Samples were washed thrice with PBS and then were blocked with solution of 1% (w/v) bovine serum albumin (BSA) in PBS containing 22.5 mg/mL glycine and 0.1% tween 20 for 1 h at room temperature. The samples were then washed with PBS thrice and incubated in 1/200 dilution of the first antibodies (Abcam) against osteopontin (OPN, ab69498), bone sialoprotein (BSP, ab52128), RUNX2 (ab76956), and collagen I (ab34710) in 0.1% (w/v) BSA in PBS solution overnight at 4°C. Samples were washed and incubated with the secondary antibody goat anti-mouse immunoglobulin G (IgG) H&L (Alexa Fluor® 488) (ab150117) and goat antirabbit IgG H&L (Alexa Fluor 594) (ab150080) and 4',6diamidino-2-phenylindole with the dilution factors of 1/500 and 1/1000, respectively, for 1 h at 37°C. Samples were washed and imaged using a confocal microscope (Zeiss LSM 800).

ALP activity assay. The osteogenic activity of the scaffolds in supporting osteogenic differentiation of MSCs and inducing mineral deposition from the differentiated cells was evaluated by ALP activity assay and xylenol orange staining.

The ALP activity of seeded cells on constructs was measured using an ALP assay kit (Colorimetric; Abcam, ab83369) according to the manufacturer's instructions. Briefly, $80\,\mu\text{L}$ of the conditioned culture media of samples was added to $50\,\mu\text{L}$ of $5\,\text{mM}$ p-nitrophenyl phosphate solution as a phosphatase substrate for ALP and was incubated at room temperature for 1 h. The absorption of the solution was measured at $405\,\text{nm}$ using the same BioTek spectrophotometer.

Xylenol orange staining. To assess the mineralization and, in particular, calcium deposition on the 3D printed scaffolds by cells, xylenol orange staining was carried out. A 20 mM stock solution was prepared by dissolving xylenol orange powder (Sigma-Aldrich, St. Louis, MO) in distilled water, and was sterile filtered. A concentration of 20 µM of stock solution in cell culture media was directly applied on cell-seeded scaffolds within multiwall plates and incubated for 12 h. Samples' culture media were changed after incubation time with the fresh one and imaged using the same confocal microscope at 570 nm (excitation)/610 nm (emission). The degree of mineralization in images was calculated as $FI \times A_{Calcify}/A_{Total}$, where FI was the fluorescence intensity, A_{Calcify} was the calcified area, and A_{Total} was the total view of the image. This degree of mineralization was computed by Matlab from five samples from each test group.

Statistical analysis

Results are presented in the form of mean \pm standard deviation of independent measurements. Statistical analyses were conducted in Minitab with 95% confidence intervals (α =5%). Statistical significance between treatments is denoted with an asterisk in the corresponding figures. Analysis of variance testing was conducted with Dunnett *post hoc* analysis for the biocompatibility testing. *t*-Tests were utilized for the comparison of the two geometric result groups

(8 mm/s and the desirable linear print speed for a composition, temperature, and pressure combination) and to compare compression testing results between molded and printed samples for a composition.

Results and Discussions

Rheological measurements

Since thermoplastic polymers such as PCL, poly (lactic acid), and poly (lactic-co-glycolic acid) are generally biologically inert, inorganic fillers such as tricalcium phosphate and HAp are commonly used to create biocomposites for bone tissue applications. However, the addition of such fillers modifies the rheological properties of the parent polymer matrix. In most cases, as reported in the literature, the addition of fillers increases the viscosity of the polymer melt due to their high surface area. Therefore, it is imperative to quantify the rheological properties of the newly prepared composites before printing.

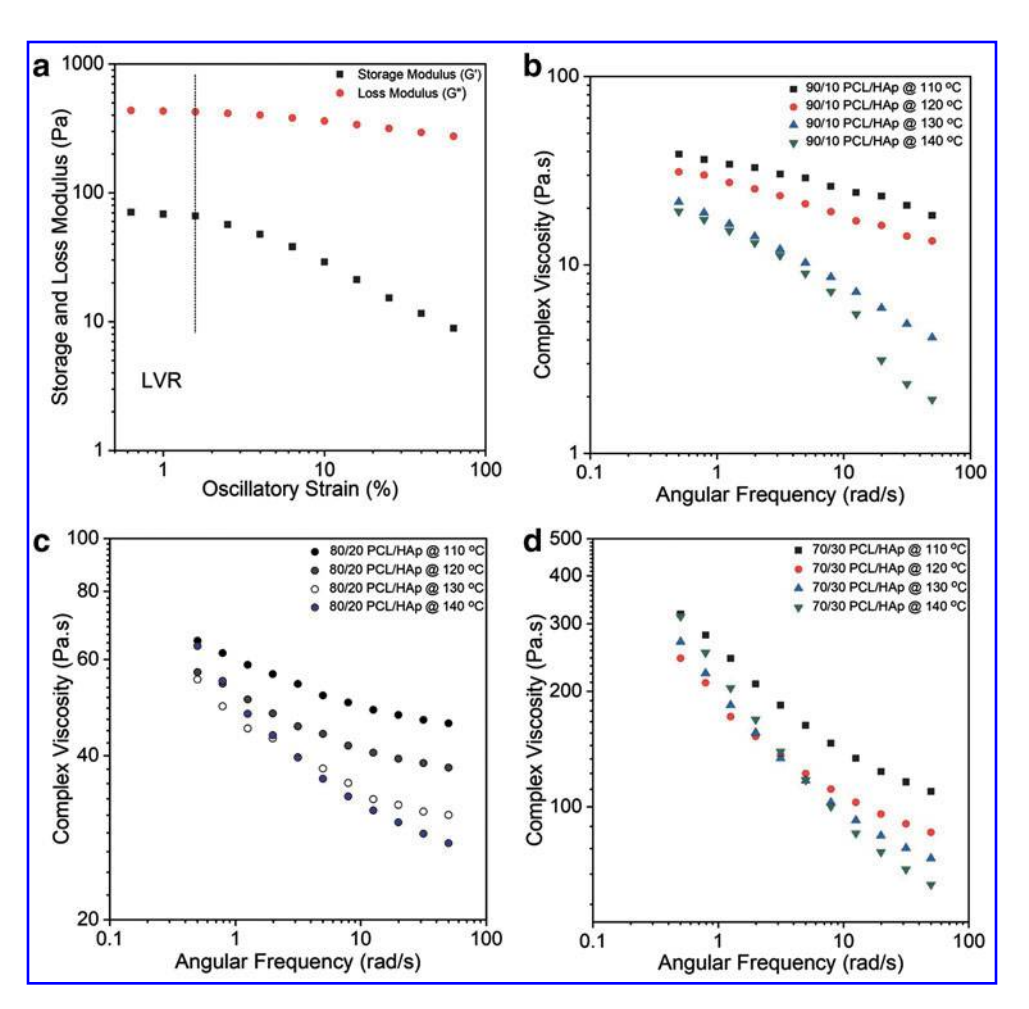
The identification of the LVR before oscillatory measurements is necessary to isolate regimes where the structure of the material will remain intact without signs of breakdown. As observed in Figure 2a, the results from the amplitude sweep revealed that the storage modulus (G') remained nearly constant for low strain values and decreased dramatically at higher strain percentages. The limit of the linear viscoelastic region (LVR) was defined as the point at which the modulus starts to decrease precipitously. Accordingly, a strain of 0.5% (within the LVR) was used for the rest of the experiments.

Results of the first set of frequency sweep experiments (Fig. 2b) revealed that the complex viscosity of 90/10 PCL/HAp at low frequencies (<1 rad/s) was in the range of 20–50 Pa·s. The relatively lower viscosity of the 90/10 PCL/HAp was because the rheology was predominantly determined by the polymer phase, and therefore experienced negligible flow resistance. As observed for 90/10 PCL/HAp, the complex viscosities for 80/20 PCL/HAp and 70/30 PCL/HAp also decreased with an increase in temperature (Fig. 2c, d). The increase in temperature was a factor capable of minimizing the influence of filler in resisting flow.

This reduction of viscosity was attributed to the relaxation of molecular entanglement of the long polymer chains at elevated temperatures. Similarly, the reduction in viscosity makes it easier for the polymer melt to flow through the conical nozzle and as a result, improves its printability. In addition, it was observed that the increase in HAp concentration also caused a considerable increase in viscosity. For example, at 110° C, the complex viscosities (at 0.5 rad/s) for 90/10, 80/20, and 70/30 PCL/HAp content were \sim 40, 90, and 330 Pa \cdot s respectively.

In this work, HAp particles (>2.5 μ m) evidently increased the viscosity of the polymer melt. For instance, tests at 110°C suggested that there was a viscosity increase of ~90% between 90/10 PCL/HAp and 70/30 PCL/HAp compositions, a common occurrence reported in rheological studies using nanocomposites.³⁴ Based on visual observations, it was also suggested that the agglomeration of HAp particles could have partly contributed to this increase. In this study, at all temperatures, all the composites evidently displayed shear-thinning behavior. For example, the values

FIG. 2. Rheological assessment of the prepared PCL/HAp composites. (a) Amplitude sweep performed at 110°C and 1 Hz to identify the LVR region of the 70/30 PCL/HAp composite. (b) Frequency sweep of 90/10 PCL/HAp composite performed at a frequency range of 0.5–100 rad/s at various printing temperatures (110°C, 120°C, 130°C, and 140°C). (c) Frequency sweep of 80/20 PCL/HAp carried out at the different printing temperatures. (d) Frequency sweep of 70/30 PCL/HAp carried out throughout the range of the printing temperatures. LVR, linear viscoelastic region.



dropped from 90 Pa \cdot s to 40 Pa \cdot s and from 110°C to 140°C for 80/20 PCL/HAp.

Two coefficients, consistency index (K) and flow behavior index (n), describe the shear-thinning ability of a material. While K can be used as a measure to compare viscosities of different materials, decrease in n values suggests a greater shear-thinning behavior. The quantification of shear-thinning behavior also suggested that as temperature increased, the shear-thinning behavior intensified. In this study, all the composites prepared and tested showed a classic pseudoplastic behavior as evidenced by values of n between 0 and 1 (Supplementary Table S1). As expected, the loss modulus (G') of all composites at all tested temperatures was lesser than the storage modulus (G") throughout the tested frequency range. From these results, it is reasonable to expect that higher printing temperatures facilitate extrusion, given the reduction in viscosity and shear-thinning behavior.

Print quality metrics

Linear print speed assessment. Strands were printed for the PCL/HAp mixtures at each process condition, imaged in situ by the EnvisionTEC 3D-Bioplotter's onboard camera, and strand diameters were measured in post. A decreasing average strand diameter with increasing linear print speed is evident in Figure 3a–c. This trend is likely closely related to the material extrusion rate. For instance, strands larger than the needle diameter are produced when the extrusion rate surpasses the linear print speed, causing excess material to extend outwards, ahead, and to the sides, of the print direction. Conversely, strand diameter is less than the needle diameter when the linear print speed surpasses the material extrusion rate, as a smaller volume of material is deposited at a particular point. Another explanation is that the strand thins to a lesser diameter as it is rapidly pulled along as it is being deposited.

If the resulting desirable linear print speed was below 5 mm/s, or above 40 mm/s, the PCL/HAp mixture was not subjected to geometric shape validation tests for that process condition. This serves to limit testing to a range that could be suitable for the production of large scaffolds. For traditional 3D printing, excessively slow speeds are avoided as they increase production time significantly. In addition, excessively high speeds may lead to more pronounced errors and vibration, and wear of machine elements. For instance, a bubble in the material can cause underextruded gaps in strands, which will become exacerbated at faster print speeds.

These tests revealed that certain printing conditions were infeasible for further printing and were subsequently eliminated as the combination was unviable for further testing. For instance, in Figure 3a–c, the 90/10 PCL/HAp composition at 140°C temperature and 4.5 bar of pressure yielded a strand of acceptable diameter at a linear print speed above the inordinately high printing speed 40 mm/s. Likewise, during the testing of 60/40 PCL/HAp, even the highest

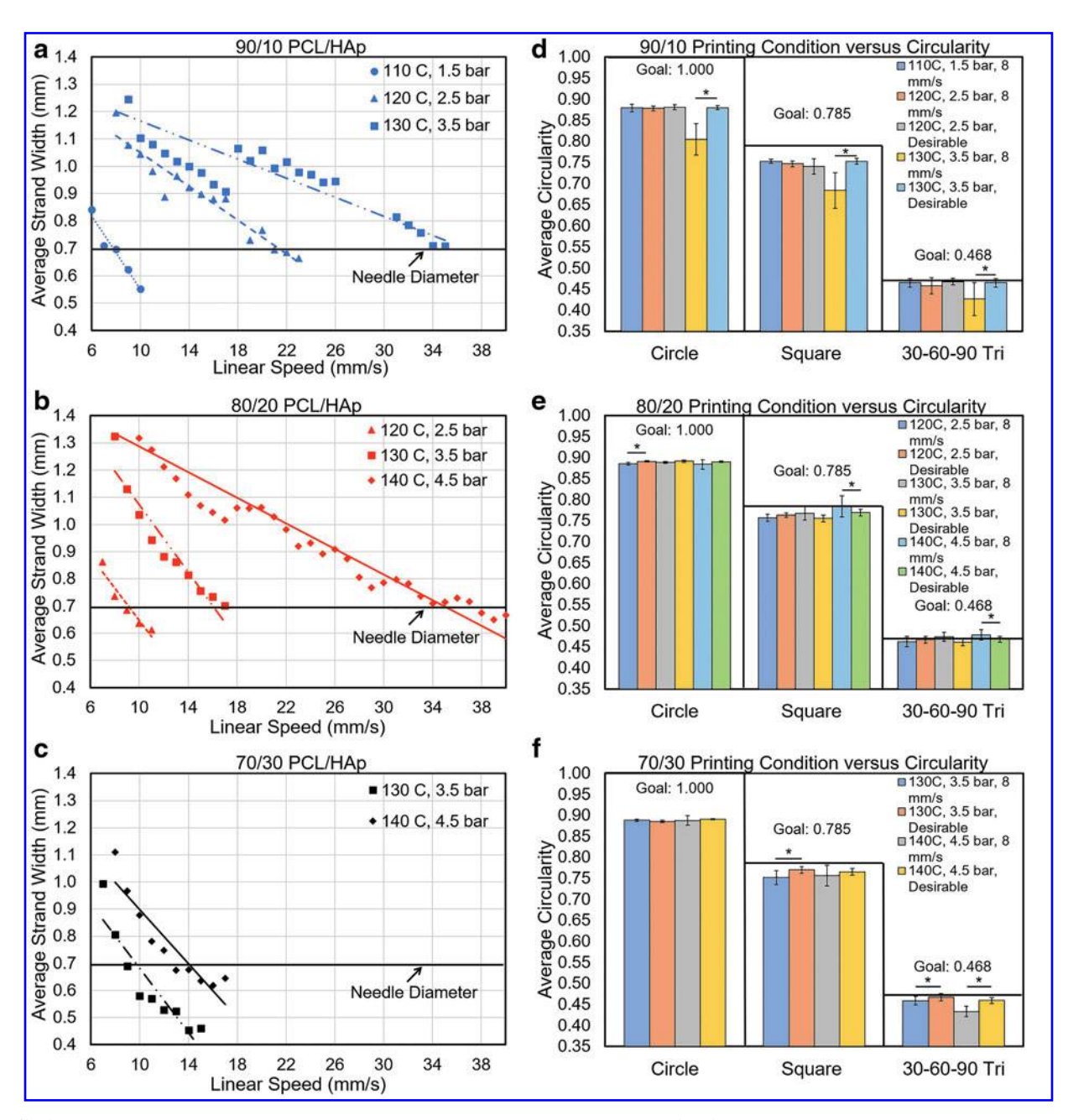


FIG. 3. Printability analysis of PCL/HAp at several composition ratios. (**a–c**) Linear speed optimization strand width results for PCL/HAp mixture ratios at different printing temperature/pressure conditions. (**d–f**) Geometric quality assessments of different composite PCL/HAp ratios printed at the linear print speeds of 8 mm/s and the desirable linear print speed for the mixture at specific printing temperature/pressure combinations (n=10; $\alpha=5\%$ for the comparison of samples printed at 8 mm/s and the desirable linear print speed for a composition).

temperature-pressure parameter combination of 140°C and 4.5 bar of pressure could not produce the desired strand width above the lowest considered linear print speed of 5 mm/s.

Accordingly, the 60/40 PCL/HAp composition was rejected as infeasible and not tested further. Comparing the three compositions in Figure 3, at a constant process temperature-pressure combination of 130°C and 3.5 bar of pressure, it becomes evident that as the proportion of the HAp increases, the desirable linear speed, and the slope of the linear print speed to average strand width relationship decreases. This trend stems from the increase in viscosity of the

composite with increasing bone material (HAp), which in turn reduces the extrusion rate of the material. Images used in the linear print speed analysis can be seen in Figure 4. Approximately desirable linear print speeds determined as the closest linear print speed yielding strand widths near 0.7 mm are shown in Supplementary Table S2.

Geometric quality analysis. Three shape types (circles, squares, and 30°-60°-90° triangles) were printed at 8 mm/s (the desirable linear print speed of 90/10 PCL/HAp at 110°C and 1.5 bar) and the desirable speed for each PCL/HAp mixture for a process condition verified from the linear print

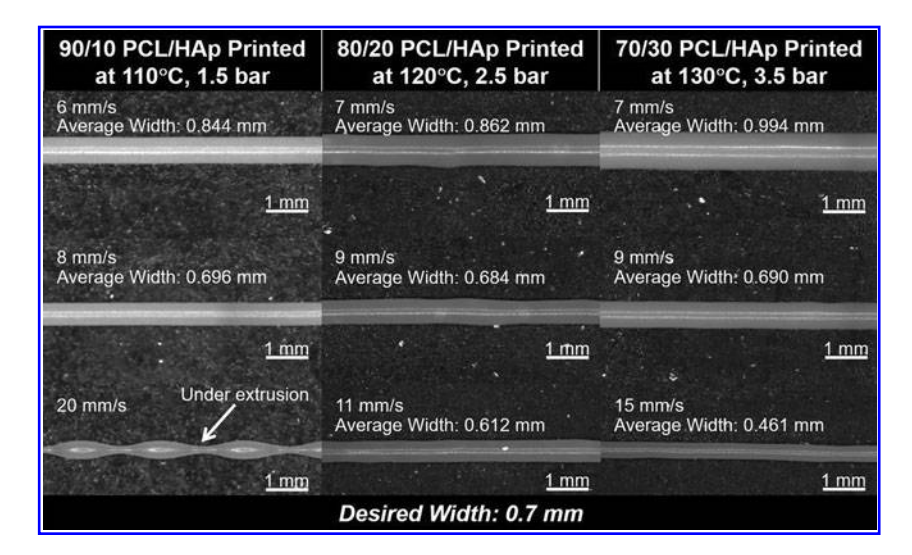


FIG. 4. *In situ* strand images illustrating the change in strand width with changes in linear print speed.

speed optimization. These shapes were chosen to approximate commonly used geometries in bioprinting, such as curvatures, sharp angle changes, and acute angles. Geometric quality was assessed using the circularity of the printed circles, squares, and $30^{\circ}-60^{\circ}-90^{\circ}$ triangles. The theoretical circularity values of circles, squares, and $30^{\circ}-60^{\circ}-90^{\circ}$ triangles are 1, 0.785, and 0.468, respectively.

Printing was conducted both at the desirable linear print speed for a mixture/process condition combination, as well as at 8 mm/s, the desirable linear print speed for 90/10 PCL/HAp at 110°C and 1.5 bar of pressure. As shown in Figure 3d–f, the printed shapes had approximately the desired circularity for all mixtures and process conditions tested, with the overall worst performing structures being circles. Comparing the geometry results in terms of circularity between geometries printed at 8 mm/s versus the desirable linear print speed for a process condition, there were statistically significant differences for some groups, most notably, the 90/10 PCL/HAp groups printed at 130°C and 3.5 bar of pressure ($\alpha = 5\%$).

Comparatively, the other compositions with statistical differences between the 8 mm/s and desirable linear print speed groups demonstrate a smaller overall difference than the 90/10 PCL/HAp groups. This difference indicates a lower geometric quality in one of the two groups, the 8 mm/s (overextrusion case) and the desirable speed, but the overextrusion case is most often the group with the inferior performance. Ultimately, for several process conditions and composite combinations, there is no statistical difference between 8 mm/s and desirable linear print speed samples. However, using a linear print speed that is lower than the desirable speed, determined by the strand diameter testing, will lead to a larger than desired strand diameter, as shown in Supplementary Figures S1 and S2. Therefore, for the printing of complex architectures, it is necessary to ensure geometric quality, since small errors can close pore spaces and inhibit nutrient flow to areas of the print.

Mechanical testing

Compressive testing results. Four samples were tested for the lowest and highest print conditions per material composition (Supplementary Table S3), and the average

compressive moduli were determined. Through visual comparison of the lower and higher printing condition's results in Figure 5, it was observed that the higher printing temperature and pressure generally yielded a higher compressive modulus for the 90/10 and 70/30 PCL/HAp compositions. Furthermore, Figure 5b shows a trend of decreasing compressive modulus with increasing HAp concentration in the printed samples. This is an unexpected outcome as the addition of hard ceramics such as HAp usually leads to an increase of the compressive modulus, as was discussed in Section "Rheological measurements." Comparing the molded and printed samples, statistically significant differences were determined to be present in most printing conditions, as shown in Figure 5b. This major difference between the 3D printed scaffolds and the base material might be due to the formation of defects and weak points in the printed structures.

To explore the latter hypothesis, the in-process printing images were visually assessed; the poorest performing samples from each group can be seen in Figure 5c. Notably, the 90/10 PCL/HAp exhibited proper deposition for both printing conditions, while the 80/20 and 70/30 PCL/HAp mixtures had print defects in the testing groups. These defects led to a less solid print, and subsequently, a lower compressive modulus. As the samples were prepared with the desirable linear print speed determined by strand width analysis, the issue is likely a partial occlusion of flow through the needle, leading to a smaller than traditional strand diameter and the creation of large gaps in the printed construct. This is an important observation highlighting the importance of *in situ* monitoring in the printing process. Also, it stresses the importance of a proper material composition and printing protocol selection, as the occurrence of printing defects in stiffer materials may lead to the generation of constructs with poor mechanical properties.

Biological properties studies

The effect of HAp content on the adhesion, growth, and osteogenic differentiation of hMSCs was investigated. For this reason, multilayered scaffolds ($10 \, \text{mm} \times 10 \, \text{mm} \times 2.4 \, \text{mm}$ featuring opposed layers with 0.4 mm between strands, demonstrated in the SEM images of Supplementary Fig. S3) from various compositions of PCL and HAp were 3D

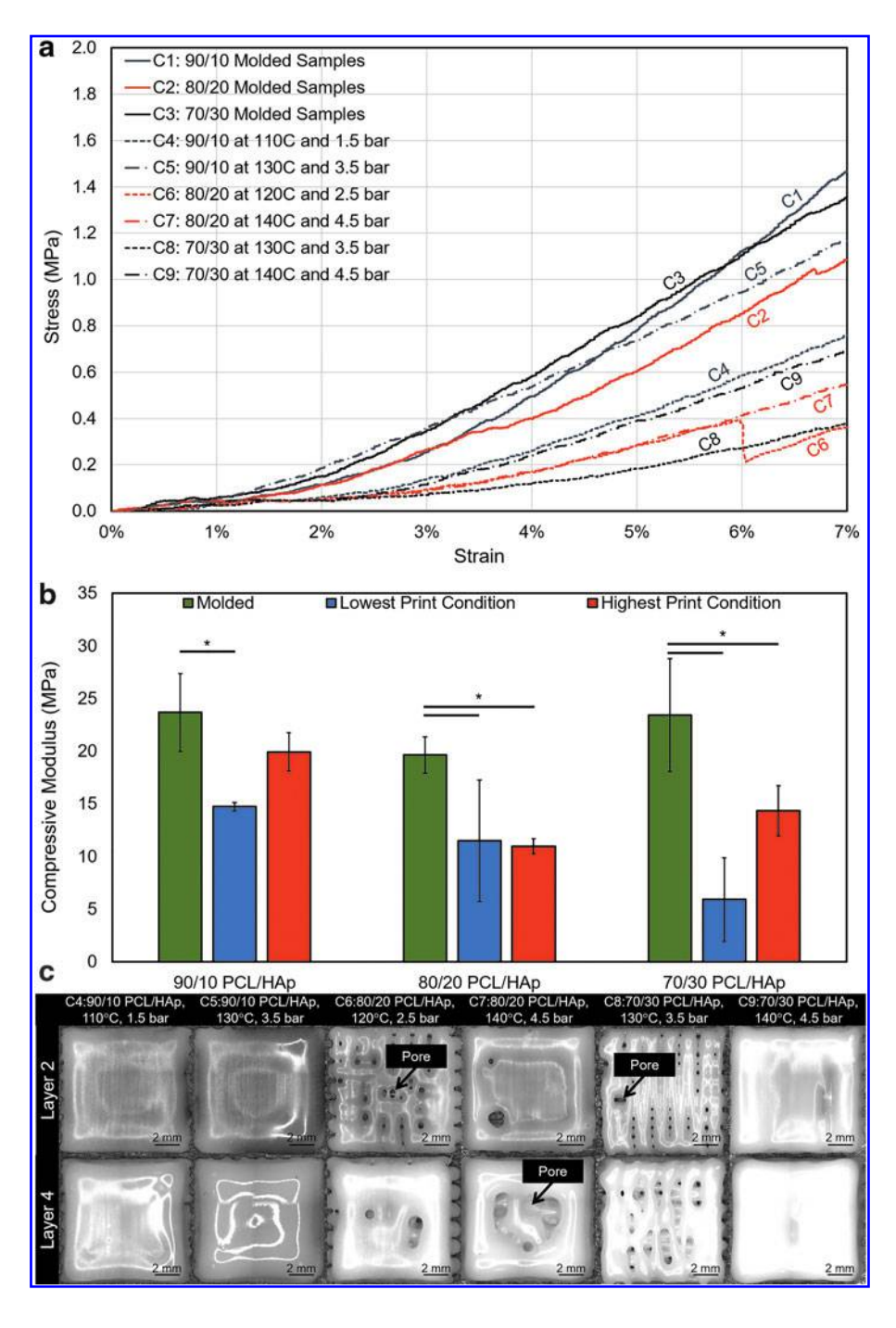


FIG. 5. Compression testing results of molded and printed PCL/ HAp. (a) Compressive behavior of representative samples for PCL/ HAp combinations, which were either molded or printed at the lowest and highest print condition under consideration for a PCL/HAp composition. (b) Average compressive modulus results of each PCL/HAp mixture ratio and compression sample preparation method (n=4 per group; $\alpha=5\%$ for the comparison of printed and molded samples for a composition). (c) In situ images from the lowest performing compressive modulus sample from each PCL/HAp composition at the lowest and highest printing condition arrangements. Statistically significant differences are denoted by an asterisk; $\alpha = 5\%$.

printed, and hMSCs were seeded on them. The cell-seeded scaffolds were used to confirm their biocompatibility and bioactivity as an osteogenic scaffold.

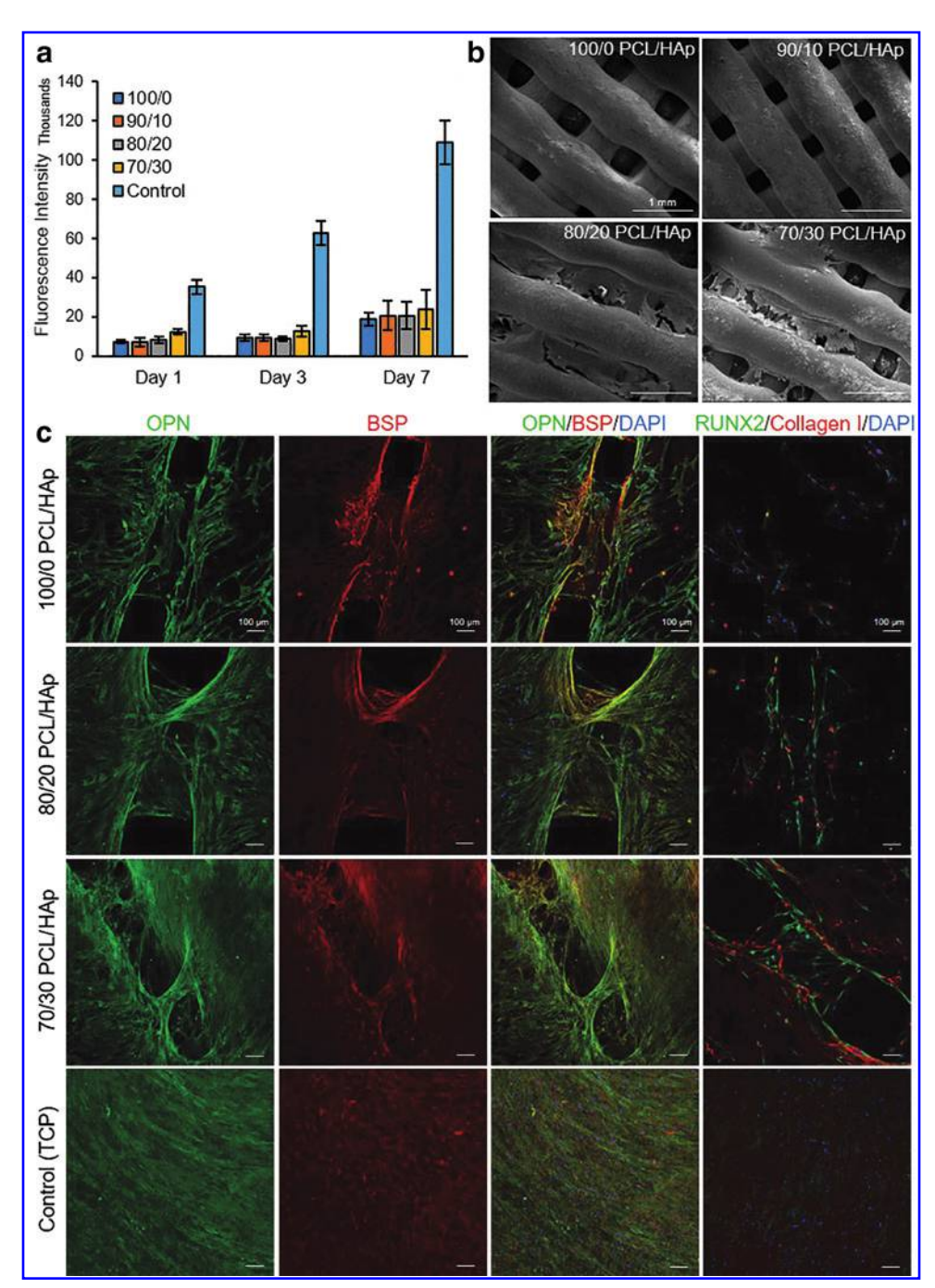
Cell attachment and viability. The proliferation rate of cultured hMSCs on the printed composite materials was assessed by PrestoBlue Cell Viability Reagent on day 1, 3, and 7 of culture (Fig. 6a). The results showed an increase in metabolic activity, suggesting the proliferation of cells during the culture period. The slight difference between 100/0 and 70/30 PCL/HAp suggests the positive role of HAp in supporting cell attachment and proliferation.

Cells were imaged using an SEM to evaluate their morphology on day 28 of the culture in differentiation media

(Fig. 6b). Although cell attachment was observed on all composite surfaces, cells qualitatively elongated more and made cellular layers on scaffolds with higher HAp content. This is probably due to the hydrophilic nature of HAp, rendering the surface of the filaments more suitable for cellular adhesion. In addition, HAp facilitates the absorption of proteins, and thus, it might facilitate the interaction of cells and scaffolds.

Assessment of cellular differentiation and mineralization. The osteogenic properties of the 3D printed composite constructs were evaluated by the assessment of hMSCs' fate when cultured on 3D printed scaffolds. The osteodifferentiation of cells was evaluated by immunostaining against

FIG. 6. Assessment of cell viability, attachment, and differentiation of cultured cells on the PCL/HAp samples. (a) Prestoblue viability assay for evaluation of cell proliferation rate on the samples over 7 days of culture (n=3 per group). (b) Scanning electron microscopy images of cultured cells on the samples to evaluate their attachment to the constructs, which shows higher attachment of cell to the 80/20 and 70/30 PCL/ HAp scaffolds than to the other groups. (c) Representative micrographs of immunostaining against bone markers (RUNX2 and collagen I as early and OPN and BSP as of late differentiation markers) indicating the differentiation of hMSCs. The results suggested that the confluency of cells and the intensity of markers were higher in groups with higher HAp concentration. OPN, osteopontin; BSP, bone sialoprotein; hMSC, human mesenchymal stem cell.



osteoblast markers, ALP activity assay, and xylenol orange staining of calcium content.

Immunostaining. To illustrate the differentiation of seeded hMSCs on scaffolds to osteoblasts, typical bone markers (RUNX2 and collagen I as early and OPN and BSP as late differentiation markers) were assessed by using immuno-fluorescence staining and imaging using confocal microscopy. Cellular expression of OPN and BSP after 28 days of seeding confirmed the osteogenic maturation of hMSCs (Fig. 6c). Both OPN and BSP were present in all samples, but the concentration of proteins and the confluency of differentiated cells on samples significantly increased from 100/0 to 70/30 PCL/HAp samples.

As anticipated, the expression of RUNX2 and collagen I was reduced on day 28 of culture, which is suggesting the late-stage differentiation of the cells. Overall, the intensity of these markers was significantly higher in composite material with HAp. These results confirmed that HAp acted as an osteoinductive material and improved osteodifferentiation. Furthermore, confocal microscopy of samples showed the growth of cells on the entire 3D surface of the scaffolds (Supplementary Fig. S4).

Alkaline phosphatase activity assay. ALP is a family of enzymes that catalyze the hydrolyzation of organic phosphate to inorganic phosphate, which is a substrate for mineralization that can be deposited together with calcium as

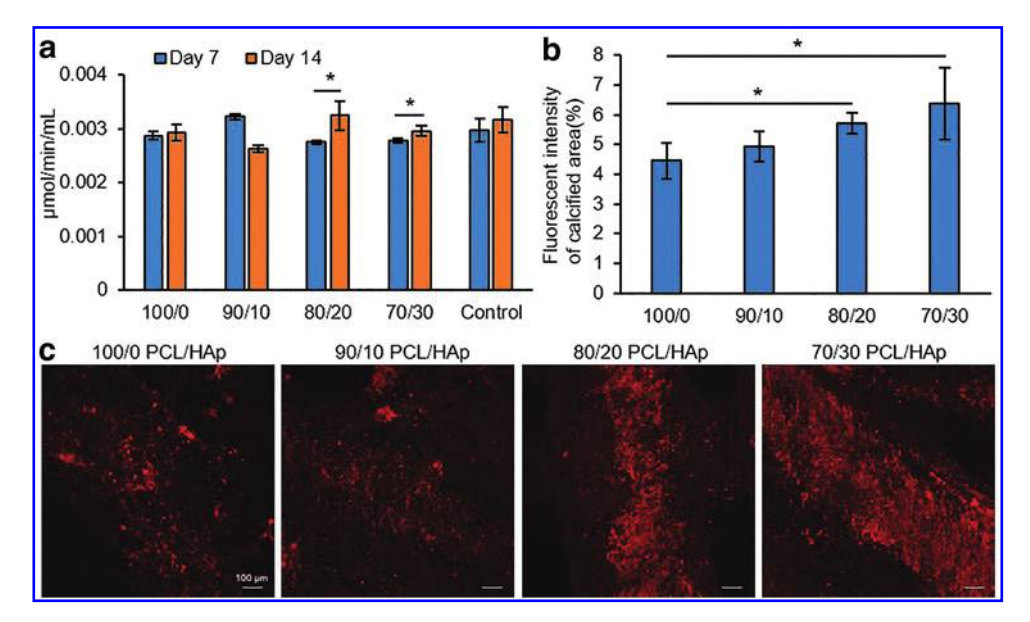


FIG. 7. Assessment of mineralization and calcium deposition of osteodifferentiated cultured cells on the PCL/HAp samples. (a) Alkaline phosphatase activity of osteoblasts on days 7 and 14 postdifferentiation, which shows that cells are differentiating; also, increasing HAp in groups cells are more directing to differentiation (n=3 per group; $\alpha=5\%$). (b) Quantified fluorescence intensity (n=3 per group; $\alpha=5\%$) and (c) confocal images of xylenol orange staining of calcium deposition of differentiated cells at day 35 postdifferentiation, which shows significant increase in groups with higher concentration of HAp.

HAp. ALP has a high activity in bones and is used as a biochemical marker of bone formation. For more evaluation of osteodifferentiation of hMSCs and their mineralization, ALP activity of cells was measured on days 7 and 14 post differentiation. We did not observe a major difference between the level of ALP activity of various groups, nor between groups and the control cells. The ALP activity significantly increased from day 7 to 14 in 70/30 PCL/HAp samples (Fig. 7a). The results suggested that HAp content of 20% (w/w) and higher had a positive role in directing the osteogenic differentiation of hMSCs.

Xylenol orange staining. Osteodifferentiated cells in the late stage of their differentiation have a high calcium deposition. To investigate the functional mineralization of differentiated cells, xylenol orange staining was performed on seeded constructs on day 35 postdifferentiation. Xylenol orange is a fluorochromatic calcium-chelating dye (red fluorescence), which was imaged using confocal microscopy (Fig. 7c). Images showed a remarkable difference in calcium deposition from 70/30 to 100/0 PCL/HAp. At the same time, we examined noncell-seeded samples of each group embedded in a culture medium, and they received fresh media during changing media of other seeded samples to examine the HAp background during the xylenol staining.

The results show a small background, which was not notable in comparison to seeded samples. Furthermore, the calcium deposition from the staining was quantified by measuring the fluorescence intensity of images (Fig. 7b). The quantification results showed that the calcification area was significantly increased by increasing the HAp percentage in the composites in comparison to pristine PCL structures. This trend suggests that the percentage of HAp positively relates to the osteogenic differentiation of the cells.

Conclusions

3D printed polymeric and composite scaffolds have shown great promise for the treatment of critically sized bone defects. As a result, numerous research efforts have been dedicated to identifying suitable compositions and architectures for such scaffolds. However, successful translation of 3D printed scaffolds to clinical practice depends on the predictability, reliability, and reproducibility of the printing process.

As a step toward successful scaling of 3D printed bone scaffolds for clinical use, in this work, we used a commercially available 3D printer for fabricating scaffolds from composites of PCL and HAp with various ratios. An instinctive approach to optimize this process is to use a statistical design of experiments, typically, using a full or fractional factorial orthogonal array. However, such an approach is time-consuming and difficult to scale, given the expensive nature of the 3D printing process. Consequently, we used a screening procedure to narrow the experimental parameter domain.

We assessed the effect of four salient parameters, namely, the composition of the bone tissue scaffold (PCL/HAp), nozzle temperature, extrusion pressure, and deposition velocity on the quality (shape and architecture) of the printed scaffolds. The composition of the PCL/HAp was tested at 70/30, 80/20, and 90/10 weight ratios. Deposition of the 60/40 composition was unviable as the material became too viscous as to be evenly extruded at the highest temperature and pressure settings possible on the machine.

Furthermore, an *in situ* monitoring system was used for gaging the printability and shape of the 3D printed scaffolds. Rheology and compressive mechanical tests were conducted, which showed that higher concentrations of HAp led to increased viscosity (negatively affecting printability) and the formation of less resilient printed scaffolds, respectively.

Our *in situ* image-based monitoring system suggested that defects generated due to improper printing process can significantly lower the mechanical properties of 3D printed polymeric scaffolds.

Finally, the biocompatibility and osteoinductivity of the scaffolds were also assessed by culturing hMSCs. While all the fabricated scaffolds were biocompatible, scaffolds with a higher concentration of HAp showed enhanced osteoinductivity. The experimental observations reported in this work suggest that, to be able to generate a predictable and reliable osteogenic material, a concentration of 20% (w/w) of HAp would be more appropriate in comparison to the compositions containing higher concentrations of HAp. This is an important observation and could be extended to other material compositions and printing processes.

Disclosure Statement

No competing financial interests exist.

Acknowledgments

The authors thank the University of Nebraska-Lincoln's Nano-Engineering Research Core Facility (NERCF) for the use of their facilities and equipment. The authors would also like to thank the Chemical Analysis Laboratory, College of Science, Rochester Institute of Technology, for the rheological characterization.

Funding Information

Financial support was from the National Science Foundation (CMMI-1719388, CMMI-1739696, and CMMI-1752069), the National Institutes of Health (GM126831, AR073822), the University of Nebraska-Lincoln, and Nebraska Tobacco Settlement Biomedical Research Enhancement Funds. Specifically, the concept of *in-situ* imaging for process monitoring and assessing the effect of process conditions on the quality of 3D printed biomaterial deposits was funded through CMMI-1739696 (Program Officer: Dr. Bruce Kramer). The National Science Foundation award also provided supplemental funding for Mr. S.G. through the Research Experience of Undergraduates program.

Supplementary Material

Supplementary Table S1

Supplementary Table S2

Supplementary Table S3

Supplementary Figure S1

Supplementary Figure S2

Supplementary Figure S3

Supplementary Figure S4

References

- Wenz, A., Borchers, K., Tovar, G.E.M., and Kluger, P.J. Bone matrix production in hydroxyapatite-modified hydrogels suitable for bone bioprinting. Biofabrication 9, 044103, 2017.
- Moncal, K.K., Heo, D.N., Godzik, K.P., et al. 3D printing of poly(ε-caprolactone)/poly(D,L-lactide-co-glycolide)/ hydroxyapatite composite constructs for bone tissue engineering. J Mater Res 33, 1972, 2018.

3. Cho, Y.S., Choi, S., Lee, S.-H., Kim, K.K., and Cho, Y.-S. Assessments of polycaprolactone/hydroxyapatite composite scaffold with enhanced biomimetic mineralization by exposure to hydroxyapatite via a 3D-printing system and alkaline erosion. Eur Polym J 113, 340, 2019.

- Heinrich, M.A., Liu, W., Jimenez, A., et al. 3D Bioprinting: from Benches to Translational Applications. Small 15, 1805510, 2019.
- Elkhoury, K., Russell, C.S., Sanchez-Gonzalez, L., et al. Soft-nanoparticle functionalization of natural hydrogels for tissue engineering applications. Adv Healthc Mater 8, [Epub ahead of print]; DOI: 10.1002/adhm.201900506, 2019.
- Nasajpour, A., Ansari, S., Rinoldi, C., et al. A multifunctional polymeric periodontal membrane with osteogenic and antibacterial characteristics. Adv Funct Mater 28, 1703437, 2018.
- Rezaei Nejad, H., Goli Malekabadi, Z., Kazemzadeh Narbat, M., et al. Laterally confined microfluidic patterning of cells for engineering spatially defined vascularization. Small 12, 5132, 2016.
- Fallahi, A., Khademhosseini, A., and Tamayol, A. Textile processes for engineering tissues with biomimetic architectures and properties. Trends Biotechnol 34, 683, 2016.
- 9. Mohammadi, M., Mousavi Shaegh, S.A., Alibolandi, M., *et al.* Micro and nanotechnologies for bone regeneration: recent advances and emerging designs. J Control Release **274**, 35, 2018.
- Kazemzadeh-Narbat, M., Rouwkema, J., Annabi, N., et al. Engineering photocrosslinkable bicomponent hydrogel constructs for creating 3D vascularized bone. Adv Healthc Mater 6, 1601122, 2017.
- 11. Ribeiro, A., Blokzijl, M.M., Levato, R., *et al.* Assessing bioink shape fidelity to aid material development in 3D bioprinting. Biofabrication **10**, 014102, 2017.
- 12. Byambaa, B., Annabi, N., Yue, K., *et al.* Bioprinted osteogenic and vasculogenic patterns for engineering 3D bone tissue. Adv Healthc Mater **6**, 1700015, 2017.
- Faramarzi, N., Yazdi, I.K., Nabavinia, M., et al. Patientspecific bioinks for 3D bioprinting of tissue engineering scaffolds. Adv Healthc Mater 7, 1701347, 2018.
- 14. Jian, H., Wang, M., Wang, S., Wang, A., and Bai, S. 3D bioprinting for cell culture and tissue fabrication. Bio-Design Manufact 1, 45, 2018.
- Skardal, A. Perspective: "Universal" bioink technology for advancing extrusion bioprinting-based biomanufacturing. Bioprinting 10, e00026, 2018.
- Nyberg, E., Rindone, A., Dorafshar, A., and Grayson, W. Comparison of 3D-printed poly-ε-caprolactone scaffolds functionalized with tricalcium phosphate, hydroxyapatite, bio-oss, or decellularized bone matrix. Tissue Eng Part A 23, 503, 2016.
- 17. Rinoldi, C., Fallahi, A., Yazdi, I.K., *et al.* Mechanical and biochemical stimulation of 3D multilayered scaffolds for tendon tissue engineering. ACS Biomater Sci Eng **5**, 2953, 2019.
- 18. Park, J.Y., Choi, J.-C., Shim, J.-H., *et al.* A comparative study on collagen type I and hyaluronic acid dependent cell behavior for osteochondral tissue bioprinting. Biofabrication **6**, 035004, 2014.
- Zhang, H., Mao, X., Du, Z., et al. Three dimensional printed macroporous polylactic acid/hydroxyapatite composite scaffolds for promoting bone formation in a criticalsize rat calvarial defect model. Sci Technol Adv Mater 17, 136, 2016.

- Ashammakhi, N., Hasan, A., Kaarela, O., et al. Advancing frontiers in bone bioprinting. Adv Healthc Mater 8, 1801048, 2019.
- Chuenjitkuntaworn, B., Inrung, W., Damrongsri, D., Mekaapiruk, K., Supaphol, P., and Pavasant, P. Polycaprolactone/hydroxyapatite composite scaffolds: preparation, characterization, and in vitro and in vivo biological responses of human primary bone cells. J Biomed Mater Res Part A 94A, 241, 2010.
- 22. Kačarević, Ž.P., Rider, P.M., Alkildani, S., *et al.* An introduction to 3D bioprinting: possibilities, challenges and future aspects. Materials (Basel) **11**, 2199, 2018.
- 23. Gungor-Ozkerim, P.S., Inci, I., Zhang, Y.S., Khademhosseini, A., and Dokmeci, M.R. Bioinks for 3D bioprinting: an overview. Biomater Sci 6, 915, 2018.
- Aljohani, W., Ullah, M.W., Zhang, X., and Yang, G. Bioprinting and its applications in tissue engineering and regenerative medicine. Int J Biol Macromol 107, 261, 2018.
- 25. Kang, K.H., Hockaday, L.A., and Butcher, J.T. Quantitative optimization of solid freeform deposition of aqueous hydrogels. Biofabrication **5**, 035001, 2013.
- Zehnder, T., Sarker, B., Boccaccini, A.R., and Detsch, R. Evaluation of an alginate–gelatine crosslinked hydrogel for bioplotting. Biofabrication 7, 025001, 2015.
- 27. Webb, B., and Doyle, B.J. Parameter optimization for 3D bioprinting of hydrogels. Bioprinting **8**, 8, 2017.
- 28. Cheng, Z., Cui, M., Shi, Y., Qin, Y., and Zhao, X. Fabrication of cell-laden hydrogel fibers with controllable diameters. Micromachines (Basel) **8**, 161, 2017.
- Ouyang, L., Yao, R., Zhao, Y., and Sun, W. Effect of bioink properties on printability and cell viability for 3D bioplotting of embryonic stem cells. Biofabrication 8, 035020, 2016.
- Soltan, N., Ning, L., Mohabatpour, F., Papagerakis, P., and Chen, X. Printability and cell viability in bioprinting alginate dialdehyde-gelatin scaffolds. ACS Biomater Sci Eng 5, 2976, 2019.
- 31. Zhang, H., Mao, X., Zhao, D., *et al.* Three dimensional printed polylactic acid-hydroxyapatite composite scaffolds for prefabricating vascularized tissue engineered bone: an in vivo bioreactor model. Sci Rep 7, 15255, 2017.

- 32. Bendtsen, S.T., Quinnell, S.P., and Wei, M. Development of a novel alginate-polyvinyl alcohol-hydroxyapatite hydrogel for 3D bioprinting bone tissue engineered scaffolds. J Biomed Mater Res Part A **105**, 1457, 2017.
- 33. Jing, X., Mi, H.-Y., and Turng, L.-S. Comparison between PCL/hydroxyapatite (HA) and PCL/halloysite nanotube (HNT) composite scaffolds prepared by co-extrusion and gas foaming. Mater Sci Eng C **72**, 53, 2017.
- 34. Nobile, M.R., Greco, F., Poggetto, G.D., d'Ayala, G.G., and Laurienzo, P. Viscoelastic behaviour of novel PCL/ hydroxyapatite nanocomposites for bone regeneration. AIP Conf Proc 1981, 020106, 2018.

Address correspondence to:
Ali Tamayol, PhD
Department of Mechanical and Materials Engineering
University of Nebraska-Lincoln
900 N 16th Street, SEC 233
Lincoln, NE 68588

E-mail: atamayol@unl.edu

Prahalada Rao, PhD
Department of Mechanical and Materials Engineering
University of Nebraska-Lincoln
900 N 16th Street, NH W342
Lincoln, NE 68588

E-mail: rao@unl.edu

Iris V. Rivero, PhD
Department of Industrial and Systems Engineering
Rochester Institute of Technology
81 Lomb Memorial Drive, Room GLE-1513
Rochester, NY 14623-5603

E-mail: iris.rivero@rit.edu

Received: September 5, 2019 Accepted: January 16, 2020 Online Publication Date: February 27, 2020

This article has been cited by:

1. Cijun Shuai, Li Yu, Pei Feng, Chengde Gao, Shuping Peng. 2020. Interfacial reinforcement in bioceramic/biopolymer composite bone scaffold: The role of coupling agent. *Colloids and Surfaces B: Biointerfaces* 193, 111083. [Crossref]